



Cite this: DOI: 10.1039/d1ta08086e

Phase-structure-dependent Na ion transport in yttrium-iodide sodium superionic conductor Na₃YI₆†

He Huang,^a Hong-Hui Wu,^a Cheng Chi,^c Yuewang Yang,^b Jiongzhi Zheng,^b Baoling Huang^{*bd} and Shouguo Wang^{*a}

All-solid-state sodium-ion batteries that utilize inorganic superionic conductors show great potential in energy storage applications. However, suitable Na superionic conductors with desirable high ionic conductivities and cross-linked diffusion networks are still in their infancy. In this work, we systematically studied the structural stabilities and Na ion transport mechanisms of the halide-based Na superionic conductors with different phase structures using first-principle calculations and data mining techniques. The iodide-based Na₃YI₆ with *C2/m*, *P3̄m1*, and *P3̄1c* space groups possess fcc and hcp anion sublattices with stable octahedral Na occupations, differing from the reported fast-ion transport mechanism in the sulfide bcc anion ones with tetrahedral Na occupations. The Oct–Tet–Oct diffusion pathway and Na-site weighted phonon vibrational frequencies play crucial roles in the synergistic Na-ion transport capabilities, leading to Na ionic conductivities of 0.35, 0.18, and 9.1×10^{-3} mS cm⁻¹ at room temperature and corresponding activation energies of 315.5, 351.1, and 454.0 meV for *C2/m*-Na₃YI₆, *P3̄m1*-Na₃YI₆, and *P3̄1c*-Na₃YI₆, respectively. Restricted by the decisive diffusion triangle, *P3̄1c*-Na₃YI₆ shows deficient Na-kinetic performance with one-dimensional blocked ion transport channels. The phase-structure-dependent ion transport networks involving Oct–Tet and Oct–Oct pathways broaden the diffusion channels and provide rational guidance for the experimental design of halide-based Na superionic conductors.

Received 20th September 2021

Accepted 1st November 2021

DOI: 10.1039/d1ta08086e

rsc.li/materials-a

Introduction

As an alternative to currently-developed lithium-ion batteries (LIBs),^{1,2} sodium-ion batteries (SIBs) gradually perform their strengths in the increasing demands of large-scale energy storage applications benefiting from the even distribution, abundant resource, and low cost of sodium metals.^{3,4} LIBs, liquid-state-electrolyte-based SIBs are suffering from inevitable troubles such as volatile flammable organics and liquid leakage.

By replacing organic liquid electrolytes with inorganic solid ones, all-solid-state SIBs could achieve a wide operation temperature range and higher energy density with direct usage of the Na metal anode and high-voltage cathodes in the battery designs. However, restricted by the sluggish ion transport in solid crystals, the effective ionic conduction of solid-state electrolytes exhibits much worse performance than that of liquid-state electrolytes (~ 1 mS cm⁻¹) at room temperature (RT).^{5,6}

Compared to currently reported Li superionic conductors (SICs) with ionic conductivities at the magnitude of over 1 mS cm⁻¹, such as sulfide Li₁₀GeP₂S₁₂ (LGPS),⁷ Li_{1+2x}Zn_{1-x}PS₄ (LZPS),⁸ oxide garnet Li₇La₃Zr₂O₁₂ (LLZO)⁹ and NASICON Li_{1.3}-Al_{0.3}Ti_{1.7}(PO₄)₃ (LATP),¹⁰ the exploit of Na SICs are still in the primary stage, mainly restricted by larger diffusive Na ionic radius. Although the Na ionic conductivity of Na₃PS₄ (~ 0.01 mS cm⁻¹, pristine)^{11,12} could be enhanced by aliovalent doping of Si, Ge, and Sn, it suffers from the narrow intrinsic electrochemical window and structural instability in contact with Na metal.¹³ Na oxides, such as NASICON Na₃Zr₂Si₂PO₁₂ and layered Na₂X₂TeO₆ (X = Mg, Zn), possess superior structural and electrochemical stabilities than sulfide,^{14–16} whereas the deficient ion diffusion channels and high sintering temperatures hinder effective Na-ion transport and increase the grain boundary impedance as well. Therefore, searching for a universal Na-ionic

^aSchool of Materials Science and Engineering, University of Science and Technology Beijing, Beijing, 100083, China. E-mail: wuhonghui@ustb.edu.cn; sgwang@ustb.edu.cn

^bDepartment of Mechanical and Aerospace Engineering, The Hong Kong University of Science and Technology, Clear Water Bay, Kowloon, Hong Kong, China. E-mail: mebhuan@ust.hk

^cKey Laboratory for Thermal Science and Power Engineering of Ministry of Education, Department of Engineering Mechanics, Tsinghua University, Beijing, 100084, China

^dHKUST Foshan Research Institute for Smart Manufacturing, Hong Kong University of Science and Technology, Clear Water Bay, Kowloon, Hong Kong, China

† Electronic supplementary information (ESI) available: Structural information of Na₃YI₆ with different phase structures; crystal structures of *c2*-Na₃YI₆ and *c2m*-Na₃YI₆; electronic band structures calculated by PBE and HSE06 hybrid functionals; mean square displacements at different temperature; Na probability distribution. See DOI: 10.1039/d1ta08086e

conduction mechanism and prospective Na SICs as good alternatives for all-solid-state SIBs is in great urgency.

Recently, the discovery of Li_3YCl_6 (space group: $P\bar{3}m1$) and Li_3YBr_6 (space group: $C2/m$) with high Li ionic conductivity over 1 mS cm^{-1} at RT,¹⁷ as well as with wide electrochemical window and structural formability, unlocked the research of halide-based SICs as a new family of Li solid-state electrolytes.^{18–21} Subsequently, Mo *et al.* conducted detailed theoretical investigations on Li-ion transport and electrochemical evaluation of halide-based Li SICs using first-principles calculations.²² Meanwhile, Sun *et al.* reported a new chloride-based SIC $\text{Li}_3\text{-InCl}_6$ with superior Li-ionic conductivity exceeding 1 mS cm^{-1} at RT *via* both ball-milling and water-mediated techniques.^{23,24} However, it is found that the similar water-mediated Na_3InCl_6 with $P\bar{3}1c$ space group possesses inferior Na ionic conductivity of only $2.23 \times 10^{-5} \text{ mS cm}^{-1}$ at 80°C .²⁴ Herein, some questions are raised: whether the halide-based Li SICs could be transferred to the Na ones? Why the halide-based crystal with the $P\bar{3}1c$ space group shows so poor performance in Na ionic conduction? What is the ion diffusion mechanism in these halide-based crystals with different phase structures? In this work, by taking the yttrium-iodide Na_3YI_6 as a benchmark, we conducted first-principles investigations of three different Na_3YI_6 crystals with $C2/m$, $P\bar{3}m1$, and $P\bar{3}1c$ space groups and revealed distinct Na-ion transport mechanisms with both Oct–Tet and Oct–Oct diffusion pathways. We expected the theoretical studies of Na-ion transport in halide-based SICs could provide rational design principles for guiding and screening superior Na inorganic solid-state electrolytes.

Calculation details

All first-principles calculations in this work were performed using density functional theory (DFT), embodied in the software of Vienna *ab initio* simulation package (VASP) with the projector-augmented wave (PAW) method.²⁵ Generalized gradient approximation (GGA) with the Perdew–Burke–Ernzerhof (PBE) functional was selected to describe the electronic exchange–correlation energy.^{26,27} The semi-core p and s electrons were treated as the valence ones for Na and Y elements, respectively. To obtain optimized structures of Na_3YI_6 with $C2/m$ ($c2m\text{-Na}_3\text{YI}_6$), $P\bar{3}m1$ ($p3m1\text{-Na}_3\text{YI}_6$), and $P\bar{3}1c$ ($p31c\text{-Na}_3\text{YI}_6$) space groups, all the parameters set, including the plane-wave energy cut-off, energy and residual force convergencies, and electron smearing were from the recommendation made by the Material Project (MP) open database²⁸ were used to maintain good consistency and comparability. Especially, for the structure optimization, the energy and force convergence criteria were less than 10^{-5} eV and $-0.02 \text{ eV \AA}^{-1}$, with the plane wave energy cut-off of 520 eV . The BZ was sampled to $5 \times 3 \times 5$, $3 \times 3 \times 5$ and $5 \times 5 \times 3$ Γ -centered Monkhorst–Pack grids for $c2m\text{-Na}_3\text{YI}_6$, $p3m1\text{-Na}_3\text{YI}_6$ and $p31c\text{-Na}_3\text{YI}_6$, respectively. The corresponding decomposition energy of each phase was defined by the ground-state energy evaluation referred to all the existing decomposition phases in the MP database. The electronic band structures were evaluated by the Heyd–Scuseria–Ernzerhof hybrid functional (HSE06)²⁹ with spin polarization.

To evaluate the phonon dispersions of $c2m\text{-Na}_3\text{YI}_6$, $p3m1\text{-Na}_3\text{YI}_6$, and $p31c\text{-Na}_3\text{YI}_6$, the energy and residual force convergencies were increased to 10^{-8} eV and $10^{-5} \text{ eV \AA}^{-1}$, respectively. The frozen-phonon method was adopted to calculate the force constant matrix and the phonon spectra were collected by using the Phonopy package.³⁰ Especially, the average Na vibrational frequency (ω_{av}) was evaluated by the corresponding phonon frequency (ω) integration weighted by the phonon density of states (DOS),³¹

$$\omega_{\text{av}} = \frac{\int \omega \text{DOS}(\omega) d\omega}{\int \text{DOS}(\omega) d\omega} \quad (1)$$

Furthermore, the bond valence site energy (BVSE) method was adopted to obtain the Na-ionic probability distributions through the soft-BV open-source software.³² Followed by the Morse type soft bond valence interaction potential principle, the Na bond valence site energies ($E_{\text{BV}_{\text{Na}}}$) were calculated by setting a dense grid with a resolution of 0.1 \AA . The corresponding Na-ion diffusion pathways were identified based on different $E_{\text{BV}_{\text{Na}}}$ isovalue.

The Na kinetics evaluation of $c2m\text{-Na}_3\text{YI}_6$, $p3m1\text{-Na}_3\text{YI}_6$, and $p31c\text{-Na}_3\text{YI}_6$ was studied by the calculations of Na ionic conductivities and migration barrier energy with the techniques of *ab initio* molecular dynamic (AIMD) simulation and the climbing nudged elastic band (CI-NEB) method.³³ For the AIMD simulation, plane-wave energy cut-off of 340 eV and energy convergence criteria of 10^{-4} eV were selected with the Γ -centered $1 \times 1 \times 1$ k -point mesh. The $2 \times 1 \times 2$, $1 \times 1 \times 2$ and $2 \times 2 \times 1$ supercell were adopted for $c2m\text{-Na}_3\text{YI}_6$, $p3m1\text{-Na}_3\text{YI}_6$ and $p31c\text{-Na}_3\text{YI}_6$, respectively. The simulated temperature ranges were from 700 K to 1000 K . Each time step was set to 2 fs and the total simulation duration was 100 ps . A canonical NVT ensemble with fixed simulation atom number, volume, and the temperature was selected with a Nosé–Hoover thermostat.³⁴ The self-diffusion coefficient (D^*) of Na ions was calculated by the mean square displacements (MSDs) over the time scale *via* the equation³⁵

$$D^* = \frac{1}{2dNt} \sum_{i=1}^N (r_i(t+t_0) - r_i(t_0))^2, \quad (2)$$

where $r_i(t+t_0)$ and $r_i(t_0)$ are the diffusive Na ionic positions at time $t+t_0$ and t_0 , respectively, t is the total time, N is the Na atom number, and d is the diffusion dimensionality. Moreover, the activation energy (E_a) and diffusion conductivity at RT could be obtained by the Arrhenius equation and Nernst–Einstein relation,³⁶

$$E_a = -k_{\text{B}}T \ln(D^*/D_0), \quad (3)$$

$$\sigma = \frac{\rho z^2 F^2 D^*}{k_{\text{B}}T}, \quad (4)$$

where D_0 represents the diffusion pre-factor, k_{B} is the Boltzmann constant, ρ is the molar density of simulated structure, z is the Na-ion integer charge, F is the Faraday constant, and T is the absolute temperature. In the CI-NEB calculations, the diffusion paths of two adjacent equilibrium Na ions were

chosen in accordance with different Na probability distributions in $c2m$ - Na_3YI_6 , $p3m1$ - Na_3YI_6 , and $p31c$ - Na_3YI_6 . 5–7 transitional images were selected according to different diffusion paths. The corresponding parameter setting was consistent with that of structure optimization calculations.

Results and discussion

Structure and stability

Analogous to the previously reported Li_3YCl_6 with the $P\bar{3}m1$ space group, Li_3YBr_6 with the $C2/m$ space group,^{17,22} and recently synthesized Na_3InCl_6 with the $P\bar{3}1c$ space group,²¹ the comparable optimized structures of yttrium-iodide Na_3YI_6 with $C2/m$ ($c2m$ for brevity), $P\bar{3}m1$ (marked as $p3m1$), and $P\bar{3}1c$ (marked as $p31c$) space groups are exhibited in Fig. 1(a–c). The calculated lattice parameters and corresponding atomic positions are listed in Table S1 of the ESI† for reference. Furthermore, as a derivative of the $C2/m$ space group, Xu *et al.* investigated the transition metal (TM) iodides with the C_2 space group as good Li SICs.¹⁹ Therefore, the lattice comparison of Na_3YI_6 with C_2 (marked as $c2$ - Na_3YI_6) and $C2/m$ space groups as illustrated in Fig. S1.† It shows that both $c2$ - Na_3YI_6 and $c2m$ - Na_3YI_6 possess similar layered structures with crossed YI_6 octahedra layers and NaI_6 octahedra ones. Representative as a unit matrix extracted from the C_2 space group with four-layered stacking sequences, $c2m$ - Na_3YI_6 is demonstrated to have a similar atomic arrangement and close DFT-calculated decomposition energy to that of $c2$ - Na_3YI_6 , as shown in Fig. 1(e). Hence, the ion transport mechanism in $c2$ - Na_3YI_6 is

symbolically represented by the investigation of $c2m$ - Na_3YI_6 in this work.

Motivated by the sublattice effect on the ion transport in SICs,^{37–39} the anion sublattice arrangements in $c2m$ - Na_3YI_6 , $p3m1$ - Na_3YI_6 , and $p31c$ - Na_3YI_6 were investigated by the simulated X-ray diffraction (XRD) spectra exhibited in Fig. 1(c). Differing from the bcc (body center cubic) anion sublattice principle for the fast-ion transport in sulfide SICs, the I sublattice in $c2m$ - Na_3YI_6 belongs to symmetric fcc (face-centered cubic) configuration, while the I sublattices in both $p3m1$ - Na_3YI_6 and $p31c$ - Na_3YI_6 satisfy the hcp (hexagonal close-packed) ones. The different I sublattice arrangement in Na_3YI_6 would lead to a distinct ion-transport mechanism from that in the bcc anion sublattice, such as the Li-ion diffusion in LGPS and $\text{Li}_7\text{P}_3\text{S}_{11}$.³⁷ Furthermore, for all studied phase structures of Na_3YI_6 , the equilibrium Na vacancy occupancies are 0.4 with additional different vacancy arrangements between the YI_6 and NaI_6 octahedra, indicating possible Na superionic conduction and distinct diffusion pathways in $c2m$ - Na_3YI_6 , $p3m1$ - Na_3YI_6 , and $p31c$ - Na_3YI_6 .

The decomposition energies, namely the energies above the hulls, assessing the decomposition tendency of the calculated compounds to their nearby decomposition phases, were evaluated by constructing the Na–Y–I ternary composition phase diagrams *via* the Material Project (MP) database. Normally, the stable phase corresponds to energy right on the hull with the decomposition energy (E_{decomp}) of 0 eV, while it is more prone to decompose when the E_{decomp} is higher. As shown in Fig. 1(d), including the C_2 phase, all the considered phase structures of

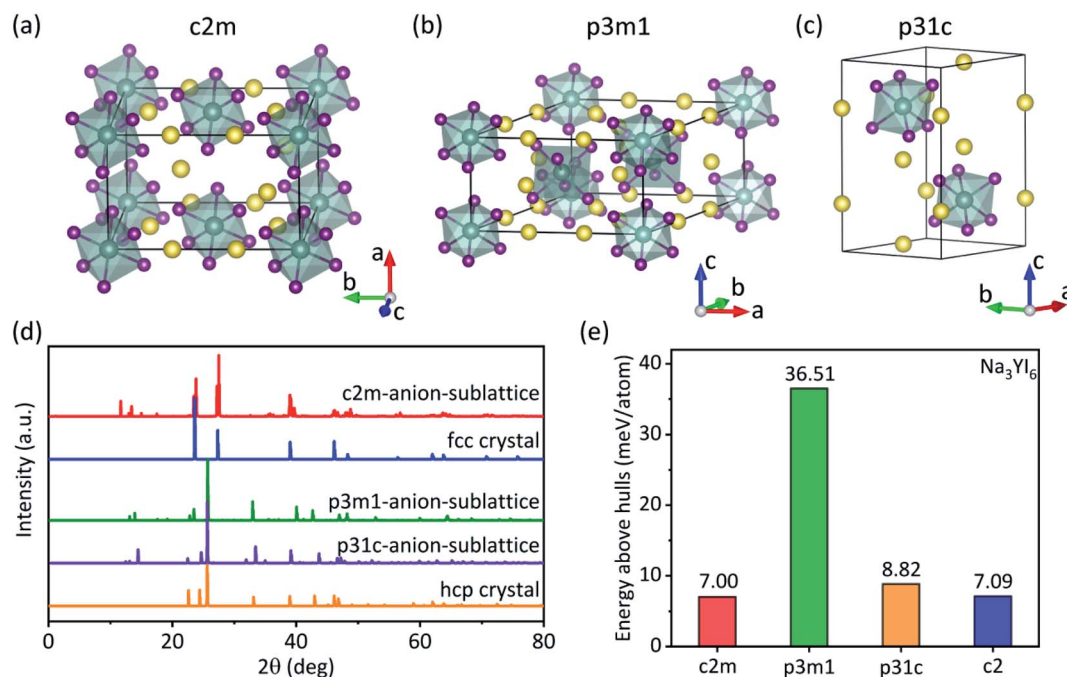


Fig. 1 Optimized atomic structures of (a) $c2m$ - Na_3YI_6 , (b) $p3m1$ - Na_3YI_6 , and (c) $p31c$ - Na_3YI_6 displayed by VESTA software. The cyan polyhedrons represent YI_6 octahedra, and the yellow, cyan, and purple balls represent Na, Y, and I atoms, respectively. (d) The simulated X-ray diffractions of the I anion sublattices in $c2m$ - Na_3YI_6 , $p3m1$ - Na_3YI_6 , and $p31c$ - Na_3YI_6 , compared with those of fcc and hcp crystals. (e) Calculated above-hull energies of the $c2m$ - Na_3YI_6 , $p3m1$ - Na_3YI_6 , $p31c$ - Na_3YI_6 , and $c2$ - Na_3YI_6 .

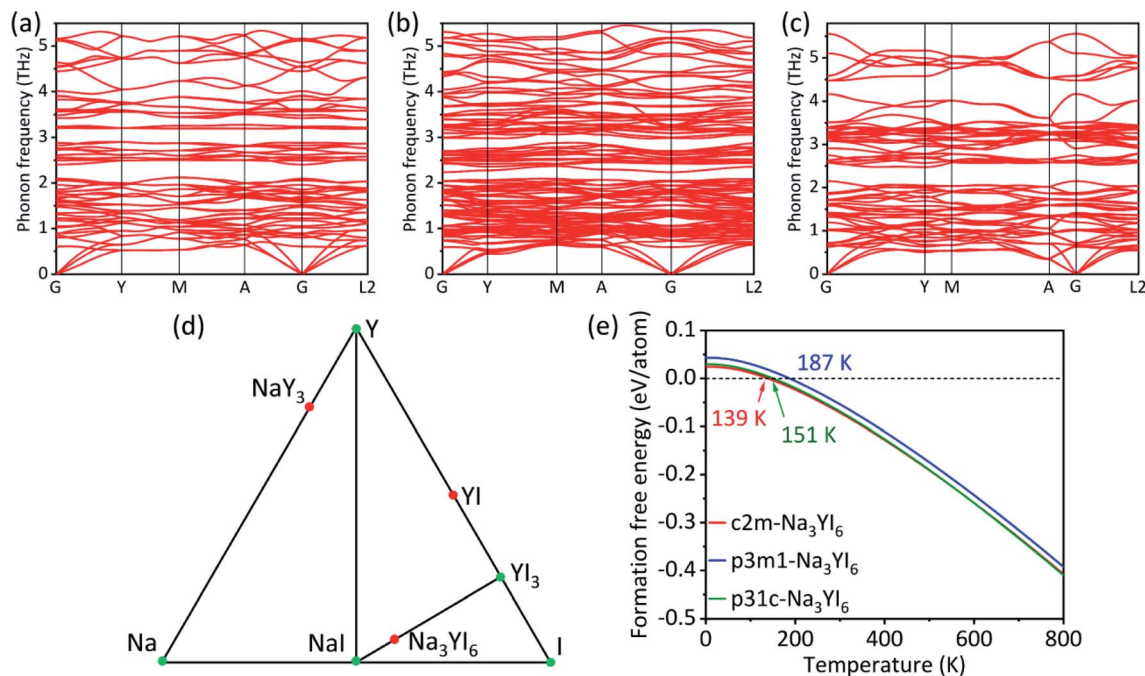


Fig. 2 Phonon spectra of (a) $c2m$ - Na_3YI_6 , (b) $p3m1$ - Na_3YI_6 , and (c) $p31c$ - Na_3YI_6 . (d) Calculated ternary Na–Y–I phase diagram at 0 K. The green and red dots represent the stable ($E_{\text{decomp}} = 0$) and unstable ($E_{\text{decomp}} > 0$) phases, respectively. The unstable Na_3YI_6 is prone to decompose to NaI and YI_3 . (e) Formation free energies of $c2m$ - Na_3YI_6 , $p3m1$ - Na_3YI_6 , and $p31c$ - Na_3YI_6 with the temperature ranging from 0 K to 800 K. It is observed that the $c2m$ - Na_3YI_6 , $p3m1$ - Na_3YI_6 , and $p31c$ - Na_3YI_6 could be thermally stable over the temperature of 139 K, 187 K, and 151 K, respectively.

Na_3YI_6 show positive values of the energies above hulls, indicating all of them are meta-stable to decompose into NaI and YI_3 at 0 K, as shown in Fig. 2(d). It is worth noting that the E_{decomp} of $c2m$ - Na_3YI_6 and $p31c$ - Na_3YI_6 are only 7.00 and 8.82 meV per atom, respectively, which are much lower than the energy contributed by the entropy at room temperature (~ 26 meV per atom) and thus indicate they are much likely to be synthesized with the consideration of the entropy effect. The dynamic stabilities of $c2m$ - Na_3YI_6 , $p3m1$ - Na_3YI_6 , and $p31c$ - Na_3YI_6 were evaluated by the phonon dispersion calculations. As shown in Fig. 2(a–c), there are no imaginary frequencies observed in $c2m$ - Na_3YI_6 , $p3m1$ - Na_3YI_6 , and $p31c$ - Na_3YI_6 , indicating all of them are dynamically stable. Meanwhile, by calculating the vibrational entropies of studied phase structures and corresponding decomposition phases YI_3 and NaI, the formation free energies of $c2m$ - Na_3YI_6 , $p3m1$ - Na_3YI_6 , and $p31c$ - Na_3YI_6 could be expressed by $F_{\text{form}}(\text{Na}_3\text{YI}_6) = F(\text{Na}_3\text{YI}_6) - 3F(\text{NaI}) - F(\text{YI}_3)$. Herein, $F(\text{Na}_3\text{YI}_6)$, $F(\text{NaI})$, and $F(\text{YI}_3)$ represent the free energies of Na_3YI_6 , NaI, and YI_3 at a given temperature. As shown in Fig. 2(e), with the consideration of the decomposition phases and the vibrational entropy effect, all the Helmholtz free energies of $c2m$ - Na_3YI_6 , $p3m1$ - Na_3YI_6 , and $p31c$ - Na_3YI_6 display negative values when the temperature goes below the room temperature, indicating all of them could be thermally stable at elevated temperatures even though the calculated E_{decomp} of $p3m1$ - Na_3YI_6 is 36.51 meV per atom.

As an upper bound of the electrochemical stability of the calculated structure, the insulating electronic property with a corresponding large bandgap is a predominant factor for SIC

as a good inorganic solid-state electrolyte. To this end, the electronic band structures of $c2m$ - Na_3YI_6 , $p3m1$ - Na_3YI_6 , and $p31c$ - Na_3YI_6 were calculated to investigate their electrochemical stabilities by using both the standard PBE and HSE06 hybrid functionals. As shown in Fig. S2,† all the calculated phase structures possess electronic insulating characteristics with indirect bandgaps of over 3.2 eV by using the PBE functional, which are much larger than those of sulfides and selenides, such as tetragonal- Na_3PS_4 (2.55 eV, calculated by PBE functional) and cubic- Na_3PSe_4 (1.52 eV, calculated by PBE functional).²⁸ Meanwhile, the HSE06-calculated bandgaps (in Fig. S3)† of $c2m$ - Na_3YI_6 , $p3m1$ - Na_3YI_6 , and $p31c$ - Na_3YI_6 are 4.45, 4.31, and 4.50 eV, respectively. The bands near the valence band maximum (VBM) are dominated by the I anions, indicating the preferred I^- oxidation at high voltages. While the bands near the conduction band minimum (CBM) are dominated by the Y cations, indicating the preferred Y^{3+} reduction at low voltages. The large bandgaps indicate that all studied phase structures of Na_3YI_6 present adequate electrochemical stabilities and wider chemical windows compared with those of Na sulfide or selenide ones to some extent.

Na ionic conductivity

The Na ionic conductivities of $c2m$ - Na_3YI_6 , $p3m1$ - Na_3YI_6 , and $p31c$ - Na_3YI_6 were evaluated by AIMD calculations with the temperature ranging from 700 K to 1000 K. The mean square displacements of all simulating ions were collected in Fig. S4–S6† as a reference. Apart from the obvious Na ion displacement, almost zero displacements of Y and I ions in all cases

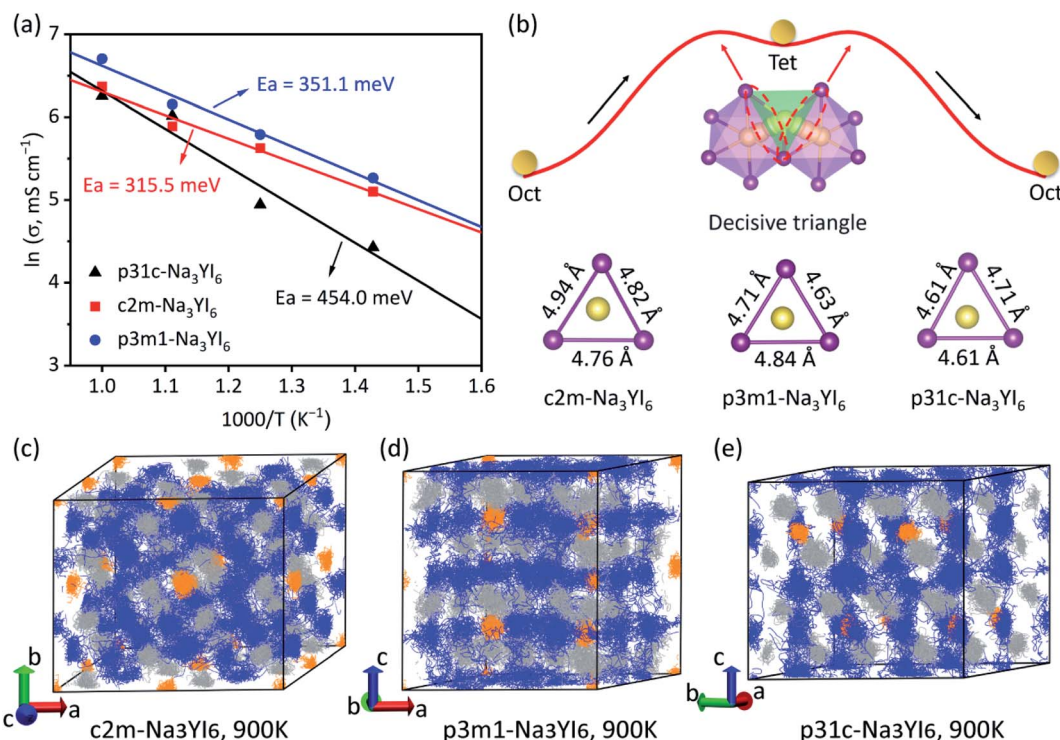


Fig. 3 (a) The Arrhenius plot of the Na ionic conductivity versus the inverse of the temperature of *c2m*-Na₃YI₆, *p3m1*-Na₃YI₆, and *p31c*-Na₃YI₆ obtained from the AIMD calculations. The correspondingly fitted Na activation energy values are labeled. (b) A schematic of Na ion diffusion from one equilibrium site to its next equilibrium site along the "Oct–Tet–Oct" path. The yellow balls represent the Na atoms, and the purple and green polyhedrons represent the NaI₆ octahedron and NaI₄ tetrahedron. The center of the NaI₆ octahedron is marked as the "Oct" site, and the center of the NaI₄ tetrahedron is marked as the "Tet" site. The maximum migration energy is determined by the difficulty that Na ion transports through the decisive triangle. The corresponding decisive triangles with marked I–I bond lengths are exhibited. (c–e) The ionic trajectories of *c2m*-Na₃YI₆, *p3m1*-Na₃YI₆, and *p31c*-Na₃YI₆ from the AIMD simulations at 900 K, plotted by the VMD software. The blue, yellow, and gray lines represent the ionic trajectories of Na, Y, and I, respectively.

demonstrate the strong Y–I interactions and thermodynamically stable skeletons to provide steady diffusion channels for Na ions, promoting the cycling performance of *c2m*-Na₃YI₆, *p3m1*-Na₃YI₆, and *p31c*-Na₃YI₆ for actual solid-state electrolyte applications.

The Arrhenius plots of *c2m*-Na₃YI₆, *p3m1*-Na₃YI₆, and *p31c*-Na₃YI₆ were plotted by assessing the Na activation energies and ionic conductivities at elevated temperatures. As shown in Fig. 3(a), the fitted Na activation energies (E_a) of *c2m*-Na₃YI₆, *p3m1*-Na₃YI₆, and *p31c*-Na₃YI₆ are 315.5, 351.1 and 454.0 meV,

Table 1 Na ionic conductivities (σ) of *c2m*-Na₃YI₆, *p3m1*-Na₃YI₆, and *p31c*-Na₃YI₆ at RT, in comparison with other, reported Na SICs

Structures	σ at RT (mS cm ⁻¹)
<i>c2m</i> -Na ₃ YI ₆	0.35
<i>p3m1</i> -Na ₃ YI ₆	0.18
<i>p31c</i> -Na ₃ YI ₆	9.10×10^{-3}
NYC ⁴⁰	0.77
NYB ⁴⁰	0.44
t-Na ₃ PS ₄ (ref. 11 and 12)	0.01
Na ₁₀ SnP ₂ S ₁₂ (ref. 44)	0.4
Na ₂ Mg ₂ TeO ₆ (exp.) ¹⁵	0.23
<i>p31c</i> -Na ₃ InCl ₆ (exp.) ²⁴	2.23×10^{-5} at 80 °C

respectively. Meanwhile, the extrapolated Na ionic diffusivities at RT were calculated to be 7.83×10^{-9} cm² s⁻¹ for *c2m*-Na₃YI₆, 3.95×10^{-9} cm² s⁻¹ for *p3m1*-Na₃YI₆, and 2.01×10^{-10} cm² s⁻¹ for *p31c*-Na₃YI₆, which could be extrapolated as shown in Fig. S8.† As a summary in Table 1, the calculated Na ionic conductivities of *c2m*-Na₃YI₆ and *p3m1*-Na₃YI₆ are 0.35 and 0.18 mS cm⁻¹, which are comparable with those of NYC (0.77 mS cm⁻¹ with error bounds of [0.12, 4.81] mS cm⁻¹),⁴⁰ NYB (0.44 mS cm⁻¹ with error bounds of [0.06, 3.22] mS cm⁻¹),⁴⁰ and Na₁₀SnP₂S₁₂ (0.4 mS cm⁻¹).⁴¹ However, worse than the *c2m*-Na₃YI₆ and *p3m1*-Na₃YI₆, the *p31c*-Na₃YI₆ crystal performs deficient Na ionic conductivity with only 9.10×10^{-3} mS cm⁻¹, which is similar to that of tetragonal-Na₃PS₄,^{11,12} and in good agreement with the poor performance of the reported *p31c*-Na₃InCl₆.²⁴

Furthermore, the thermodynamic ion transport behavior of *c2m*-Na₃YI₆, *p3m1*-Na₃YI₆, and *p31c*-Na₃YI₆ were examined by the ionic distributions during the whole AIMD simulations. Fig. 3(b–d) depicts the ionic trajectories of all simulated phase structures at 900 K. It is worth noting that, as discussed above, Y and I ions exhibit apparent vibrations around their equilibrium positions without obvious displacements, demonstrating the thermodynamically stable hosts for fast Na ion transport. The Na ionic diffusion in both the *c2m*-Na₃YI₆ and *p3m1*-Na₃YI₆

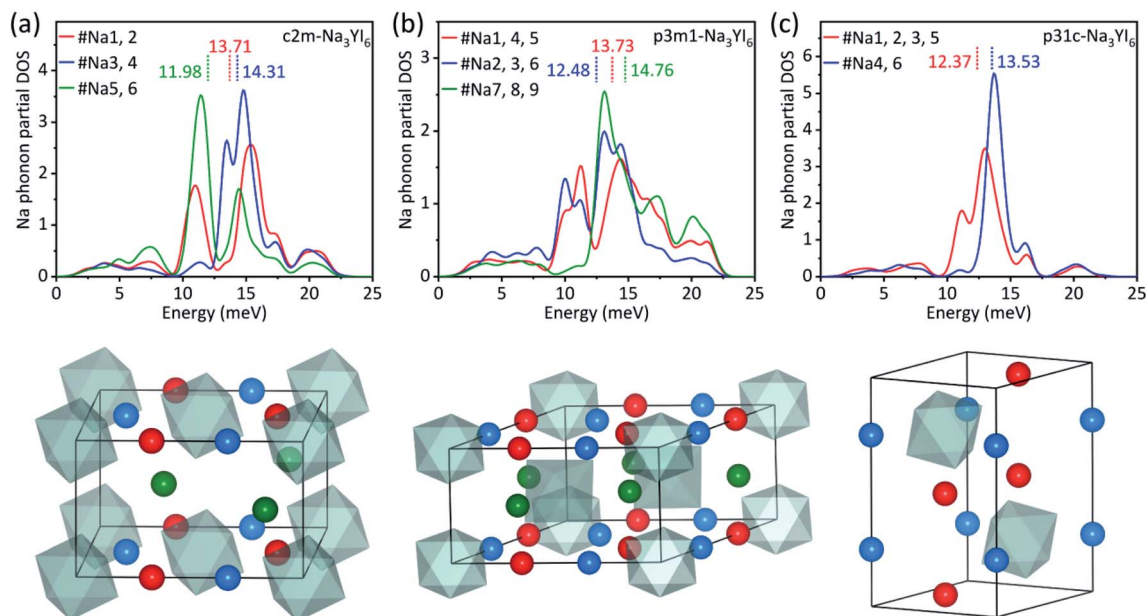


Fig. 4 Na site-weighted phonon density of states (DOS) of (a) $c2m$ - Na_3YI_6 , (b) $p3m1$ - Na_3YI_6 , and (c) $p31c$ - Na_3YI_6 with correspondingly labeled Na phonon band centers. Different types of Na ions are represented by the colored balls with corresponding-colored phonon DOS lines in the $c2m$ - Na_3YI_6 , $p3m1$ - Na_3YI_6 , and $p31c$ - Na_3YI_6 unit cell, respectively. The YI_6 octahedra are simplified as the cyan polyhedral.

follows three-dimensional cross-link networks, while Na ions diffuse along axially one-dimensional channels in the $p31c$ - Na_3YI_6 . Similar Na ionic diffusion behavior is also observed in all simulated phase structures by plotting the probability density function (P_r),⁴² which provides the most possible Na ionic distribution in the low energy (high probability) sites as revealed in Fig. S7.† Especially for the $p31c$ - Na_3YI_6 , it is found the Na ionic diffusion is severely restricted by the adjacent YI_6 octahedrons along the c -axis. The back-and-forth ionic diffusion of these Na ions contributes little to the actual effective Na ionic conductivity. Such a degraded one-dimensional Na ion diffusion manner explains the poor Na ionic conductivity of $p31c$ - Na_3YI_6 , wherein the deficient ion diffusion channels would be further blocked during the actual polycrystalline synthesis process, leading to the great grain-boundary impedance.

Phase-structure-dependent ion transport

In response to the distinct Na ion diffusion features in Na_3YI_6 with the $c2m$, $p3m1$, and $p31c$ space groups, the ion transport mechanisms behind them need to be revealed. As illustrated from the XRD pattern in Fig. 1(c), different Na ion diffusion manners stem from geometrical structural differences between $c2m$ - Na_3YI_6 , $p3m1$ - Na_3YI_6 , and $p31c$ - Na_3YI_6 . Although all phase structures of Na_3YI_6 possess the same stoichiometric compositions and similar formation energies, YI_6 octahedra arrangement with different Y cations in the octahedron sites build up the framework with distinct ion-host and energy landscapes for Na ion diffusion.

Recently, the synergic relationship between the lattice softness and corresponding ionic conductivity was reported for several SICs.^{31,43} It is believed that lower average phonon

frequencies would boost faster ion transport with fewer surroundings constraints and lower migration barriers. To this end, the phonon distributions of Na ions in $c2m$ - Na_3YI_6 , $p3m1$ - Na_3YI_6 , and $p31c$ - Na_3YI_6 were investigated by calculating the decomposed Na phonon density of states by considering different Na sites. As illustrated in Fig. 4, the Na site-weighted phonon density of states provides the distinct Na phonon frequency spectra and phonon band centers in each phase structure. In the $c2m$ - Na_3YI_6 unit cell, there are six Na atoms and three distinct Na sites, namely the #Na1, 2 (marked as the red balls), #Na3, 4 (marked as the blue balls), and #Na5, 6 sites (marked as the green balls), occupied with the calculated Na phonon band centers of 13.71, 14.31, and 11.98 meV, respectively. Similarly, there are also three distinct Na sites (#Na1, 4, 5, #Na2, 3, 6, and #Na7, 8, 9) in the $p3m1$ - Na_3YI_6 unit cell with the corresponding Na phonon band center of 13.73, 12.48, and 14.76 meV, respectively. For the $p31c$ - Na_3YI_6 unit cell, two distinct Na sites (#Na1, 2, 3, 5 and #Na4, 6) occupy the Na phonon band center of 12.37 and 13.53 meV. The detailed atomic information of all distinct Na sites is listed in Table S1† for reference. The lower Na phonon band center indicates softer bond interaction between the Na ion and the host, and thus faster ion transport. Although Na ions at the #Na1, 2, 3, 5 sites of $p31c$ - Na_3YI_6 exhibit the lowest Na phonon band centers, back and forth displacements take no effect on the overall ion diffusion because of the local Na-ion distribution blocked by adjacent YI_6 octahedra as mentioned earlier. Therefore, different from the three-dimensional Na-ion diffusion pathways with decent Na phonon band centers in both $c2m$ - Na_3YI_6 and $p3m1$ - Na_3YI_6 , the effective Na-ionic diffusion in $p31c$ - Na_3YI_6 is mainly restricted by the blocked Na-ion diffusion channel

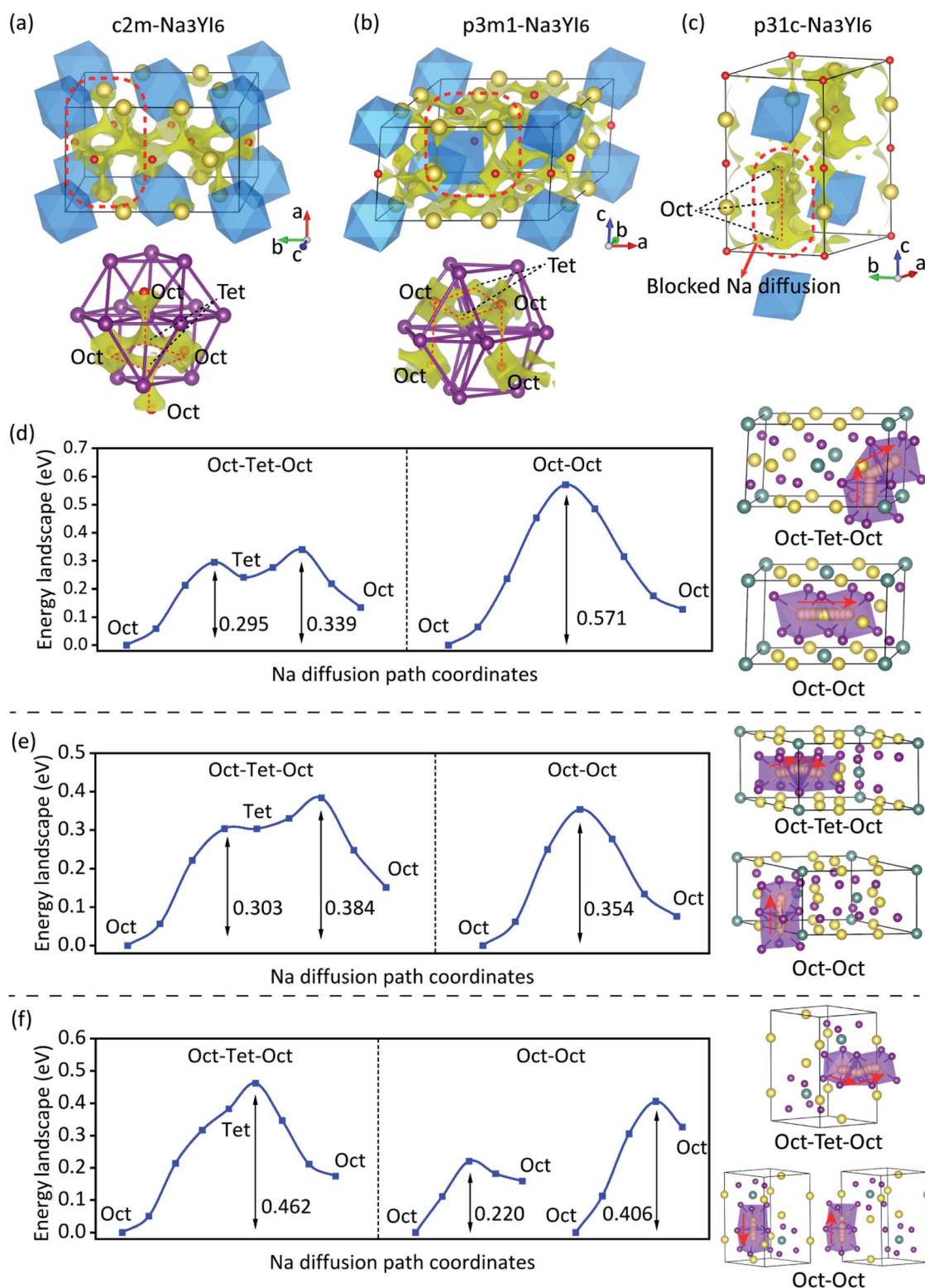


Fig. 5 Na ionic potential energy landscape of (a) $c2m\text{-Na}_3\text{Yl}_6$, (b) $p3m1\text{-Na}_3\text{Yl}_6$, and (c) $p31c\text{-Na}_3\text{Yl}_6$ by using the BVSE method. Yellow, purple, and blue polyhedral represent the Na, I, and Yl_6 octahedra, respectively. The red dots correspond to other possible Na equilibrium sites. The isosurface with yellow ribbons represents the Na ionic probability distribution. The $c2m\text{-Na}_3\text{Yl}_6$ and $p3m1\text{-Na}_3\text{Yl}_6$ exhibit three-dimensional cross-link Na ionic diffusion, while Na ionic diffusion in the $p31c\text{-Na}_3\text{Yl}_6$ mainly performs along c-axis. (d–f) The distinct Na-ionic diffusion landscape with different diffusion pathways in $c2m\text{-Na}_3\text{Yl}_6$, $p3m1\text{-Na}_3\text{Yl}_6$, and $p31c\text{-Na}_3\text{Yl}_6$ studied using the CI-NEB method. The diffusion pathways are labeled by the red arrows.

between the Na4 and Na6 sites, which greatly restricts its ion transport capability.

As discussed above, the anion sublattices of $c2m$ -Na₃YI₆, $p3m1$ -Na₃YI₆, and $p31c$ -Na₃YI₆ possess different Na-ion diffusion manners. The I sublattice occupies a face-centered cubic (fcc) arrangement in $c2m$ -Na₃YI₆, while the I sublattices in $p3m1$ -Na₃YI₆ and $p31c$ -Na₃YI₆ behave in the hexagonal close-packed (hcp) configuration. For brevity, the center of the NaI₆ octahedron is marked as the “Oct” site, and the center of the NaI₄ tetrahedron is marked as the “Tet” site. Differing from the bcc anion framework and equilibrium tetrahedron (Tet) sites in most sulfide-based SICs, equilibrium stable Na ions in $c2m$ -Na₃YI₆, $p3m1$ -Na₃YI₆, and $p31c$ -Na₃YI₆ occupy the octahedron (Oct) sites, naturally indicating different Na ion diffusion mechanisms compared to the tetrahedral diffusion manners in these sulfide-based SICs.

The BVSE method was adopted to investigate the Na ion probability distribution of $c2m$ -Na₃YI₆, $p3m1$ -Na₃YI₆, and $p31c$ -Na₃YI₆ with distinct energy landscapes and corresponding migration barriers. The Na-ion distributions with low energy isosurfaces in $c2m$ -Na₃YI₆, $p3m1$ -Na₃YI₆, and $p31c$ -Na₃YI₆ are shown in Fig. 5(a–c) with yellow ribbons, which are consistent with the Na-ion distribution obtained from the AIMD simulations, shown in Fig. S7.† Especially, it is observed that in $c2m$ -Na₃YI₆ (Fig. 5(a)), Na ions perform the cross-link diffusion network in the fcc I sublattice, wherein Na ions hop between equilibrium octahedron sites *via* transitional tetrahedron sites (Oct–Tet–Oct). While for $p3m1$ -Na₃YI₆ (Fig. 5(b)), Na ions diffuse between the equilibrium octahedron sites directly (Oct–Oct) or between the octahedron sites *via* transitional tetrahedron sites (Oct–Tet–Oct), connecting the cross-linked ionic diffusion

network in the hcp I sublattice. The ionic diffusion paths are demonstrated to differ from the expected tetrahedron site-mediated ionic diffusion (Tet–Tet or Tet–Oct–Tet) in the sulfide SICs,³⁷ illustrating octahedron site-dominated diffusion mechanism in the halide-based SICs. Similarly, it was observed that the favorable back-and-forth Na ion diffusion pathway between the octahedron sites (Oct–Oct) was blocked by the adjacent YI₆ octahedra as shown in Fig. 5(c).

Meanwhile, to evaluate the Na ion migration barriers in $c2m$ -Na₃YI₆, $p3m1$ -Na₃YI₆, and $p31c$ -Na₃YI₆, the CI-NEB method was adopted to calculate the corresponding energy landscape based on different Na-ion diffusion pathways. As shown in Fig. 5(d–f), the migration energy barrier for Na-ion diffusion along the Oct–Tet–Oct path in $c2m$ -Na₃YI₆ was calculated to be 0.339 eV, which is much lower than that along the direct Oct–Oct path (0.571 eV). It indicates that Na ions prefer to diffuse across the intermediate Tet sites when diffusing between the Oct sites. Especially, for the attempt of Na diffusion from the Oct site to the adjacent Tet site, the Na migration energy barrier is relatively lower to be 0.295 eV. For the $p3m1$ -Na₃YI₆, the energy barriers for Na ion diffusion along the Oct–Tet–Oct and direct Oct–Oct pathways are calculated to 0.384 and 0.354 eV, respectively, indicating the comparable Na ionic diffusion manners in the $p3m1$ -Na₃YI₆ along these two different pathways. Similarly, it has the same tendency that Na ion diffuses from the Oct site to its nearby Tet site with a lower energy barrier of 0.303 eV. In Fig. 5(f), although the Na-ion diffusion barrier between the Na1 and Na2 (or between Na3 and Na5) sites (direct Oct–Oct) in the $p31c$ -Na₃YI₆ is found only 0.22 eV, previously discussed back-and-forth Na ion diffusion in these sites provides little contribution to the total effective Na ionic diffusion. However, to get

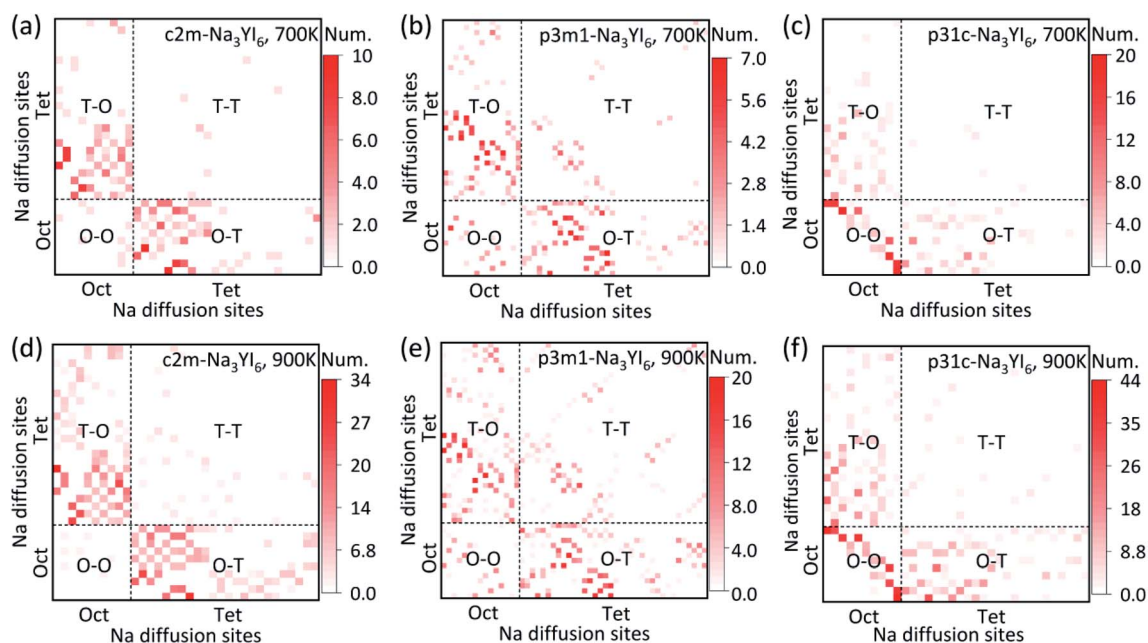


Fig. 6 Na transition number distribution hot maps of $c2m$ -Na₃YI₆ (a and d), $p3m1$ -Na₃YI₆ (b and e), and $p31c$ -Na₃YI₆ (c and f) obtained from AIMD simulations at 700 K and 900 K. The diffusive Na sites in the center of octahedron sites (Oct) and tetrahedron sites (Tet) are labeled, including distinct Oct–Oct (O–O), Oct–Tet (O–T), Tet–Oct (T–O) and Tet–Tet (T–T) ion hopping pathways.

rid of the local diffusion invalidity, Na ions need to overcome the energy barrier of 0.462 eV by getting rid of the local cage blocked by the YI_6 octahedra to the nearby Na4 or Na6 site through the Oct–Tet–Oct pathway.

Furthermore, with the data mining techniques, the dynamic Na-ion distributions in $c2m$ - Na_3YI_6 , $p3m1$ - Na_3YI_6 , and $p31c$ - Na_3YI_6 were visualized by collecting the Na-ion diffusion events in the AIMD simulations. Fig. 6 shows the Na transition number distribution hot maps with consideration of all possible Oct and Tet sites (depicted in Table S2†) in the $c2m$ - Na_3YI_6 , $p3m1$ - Na_3YI_6 , and $p31c$ - Na_3YI_6 at 700 K and 900 K. The transition numbers of Na ion diffusion along the Oct–Oct, Oct–Tet, Tet–Oct, and Tet–Tet pathways are counted during the whole simulation duration. It was observed that the Oct–Tet diffusion pathway is dominant for Na-ion hopping in the $c2m$ - Na_3YI_6 at both 700 K and 900 K, while the $p3m1$ - Na_3YI_6 has comparable distributions for both Oct–Oct and Oct–Tet type Na ion transitions, which is consistent with the calculated energy barriers in Fig. 5(e). For the $p31c$ - Na_3YI_6 , it showed that Na-ion transitions along the Oct–Oct path dominate total Na-ion diffusion in both 700 K and 900 K. Especially, when the temperature goes higher, Na ions have higher probabilities to proceed Oct–Tet type transitions and realize the effective Na ion diffusion. Therefore, it can be concluded that the Oct–Tet–Oct diffusion pathway plays a crucial role in the iodide-based Na SICs with the fcc and hcp anion sublattices. As highlighted in Fig. 3(b), the diffusion channel for the Na-ion hopping between adjacent Oct sites is highly dependent on the Oct–Tet transitional diffusion, wherein the size of the cross-sectional area, namely the decisive triangle, makes a great effect on the ease of Na-ion transport. Normally, a relatively larger and optimal diffusion channel with corresponding lower ion–ion interaction would promote faster ion transport. It is found that the areas of the decisive triangles in the $c2m$ - Na_3YI_6 , $p3m1$ - Na_3YI_6 , and $p31c$ - Na_3YI_6 are 10.136, 9.664, and 9.333 \AA^3 , respectively, which explains the activation energy, Na ionic conductivity, and decisive energy barrier differences calculated by AIMD and CI-NEB calculations.

Conclusions

In this work, by using first-principle calculations and *ab initio* molecular dynamic simulations, we systematically studied the structural stabilities and the Na-ion transport mechanism in iodide-based Na superionic conductors Na_3YI_6 with different phase structures. Compared to the reported fast-ion transport mechanism, in sulfide ionic conductors with stable tetrahedral ion configurations and preferred Tet–Tet ion diffusion path, the phase-structure dependent Na_3YI_6 with the $c2m$, $p3m1$, and $p31c$ space groups performed fcc and hcp anion sublattices with stable octahedral Na-ones and corresponding Oct–Oct and Oct–Tet ion transition manners. The Na-site weighted phonon vibrational frequencies and the determinative Oct–Tet–Oct diffusion path were found to be responsible for the distinct Na-ion transport abilities, with the Na-ionic conductivities of 0.35, 0.18, and $9.1 \times 10^{-3} \text{ mS cm}^{-1}$ at room temperature and corresponding activation energies of 315.5, 351.1, and 454.0 meV in the $c2m$ - Na_3YI_6 , $p3m1$ - Na_3YI_6 , and $p31c$ - Na_3YI_6 , respectively.

With decent, Na-ion diffusion barriers along the Oct–Tet and Oct–Oct pathways, the Na_3YI_6 crystal with $c2m$ and $p3m1$ space groups possess three-dimensional cross-linked Na-ionic diffusion networks. However, restricted by the decisive diffusion triangle along the Oct–Tet–Oct path, $p31c$ - Na_3YI_6 shows quite poor Na kinetic performance with one-dimensional ion diffusion channel and local back-and-forth Na ion diffusion blocked by adjacent YI_6 octahedra. The revealed phase structure-dependent ion diffusion networks consisting of Oct–Tet and Oct–Oct pathways broaden the fast Na-ion transport mechanism and provide rational guidance for halide-based Na superionic conductors design and synthesis.

Conflicts of interest

There are no conflicts to declare.

Acknowledgements

This work was supported by the Postdoctoral International Exchange Program (Grant No. YJ20210027), the Hong Kong Innovation and Technology Fund (Grant No. ITS/051/18), the National Key Research and Development Program of China (Grant No. 2019YFB2005800), the Natural Science Foundation of China (Grant No. 51625101, 51901013, 52071023, 52130103 and 52122408), the Beijing Natural Science Foundation Key Program (Grant No. Z190007), and the Fundamental Research Funds for the Central Universities (Grant No. 06500135).

References

- 1 B. Scrosati, *Electrochim. Acta*, 2000, **45**, 2461–2466.
- 2 J. W. Choi and D. Aurbach, *Nat. Rev. Mater.*, 2016, **1**, 16013.
- 3 J.-Y. Hwang, S.-T. Myung and Y.-K. Sun, *Chem. Soc. Rev.*, 2017, **46**, 3529–3614.
- 4 B. L. Ellis and L. F. Nazar, *Curr. Opin. Solid State Mater. Sci.*, 2012, **16**, 168–177.
- 5 J. Janek and W. G. Zeier, *Nat. Energy*, 2016, **1**, 1–4.
- 6 W. Zhou, Y. Li, S. Xin and J. B. Goodenough, *ACS Cent. Sci.*, 2017, **3**, 52–57.
- 7 Y. Mo, S. P. Ong and G. Ceder, *Chem. Mater.*, 2012, **24**, 15–17.
- 8 W. D. Richards, Y. Wang, L. J. Miara, J. C. Kim and G. Ceder, *Energy Environ. Sci.*, 2016, **9**, 3272–3278.
- 9 R. Murugan, V. Thangadurai and W. Weppner, *Angew. Chem., Int. Ed.*, 2007, **46**, 7778–7781.
- 10 M. Monchak, T. Hupfer, A. Senyshyn, H. Boysen, D. Chernyshov, T. Hansen, K. G. Schell, E. C. Bucharsky, M. J. Hoffmann and H. Ehrenberg, *Inorg. Chem.*, 2016, **55**, 2941–2945.
- 11 H. Huang, H.-H. Wu, X. Wang, B. Huang and T.-Y. Zhang, *Phys. Chem. Chem. Phys.*, 2018, **20**, 20525–20533.
- 12 I.-H. Chu, C. S. Kompella, H. Nguyen, Z. Zhu, S. Hy, Z. Deng, Y. S. Meng and S. P. Ong, *Sci. Rep.*, 2016, **6**, 33733.
- 13 Z. Zhu, I.-H. Chu, Z. Deng and S. P. Ong, *J. Mater. Chem. A*, 2015, **27**, 8318–8325.

- 14 H. Park, K. Jung, M. Nezafati, C. S. Kim and B. Kang, *ACS Appl. Mater. Interfaces*, 2016, **8**, 27814–27824.
- 15 Y. Li, Z. Deng, J. Peng, J. Gu, E. Chen, Y. Yu, J. Wu, X. Li, J. Luo and Y. Huang, *ACS Appl. Mater. Interfaces*, 2018, **10**, 15760–15766.
- 16 H. Huang, Y. W. Yang, C. Chi, H. H. Wu and B. L. Huang, *J. Mater. Chem. A*, 2020, **8**, 22816–22827.
- 17 T. Asano, A. Sakai, S. Ouchi, M. Sakaida, A. Miyazaki and S. Hasegawa, *Adv. Mater.*, 2018, **30**, 1803075.
- 18 J. Liang, X. Li, S. Wang, K. R. Adair, W. Li, Y. Zhao, C. Wang, Y. Hu, L. Zhang and S. Zhao, *J. Am. Chem. Soc.*, 2020, **142**, 7012–7022.
- 19 Z. Xu, X. Chen, K. Liu, R. Chen, X. Zeng and H. Zhu, *Chem. Mater.*, 2019, **31**, 7425–7433.
- 20 R. Schlem, A. Banik, S. Ohno, E. Suard and W. G. Zeier, *Chem. Mater.*, 2021, **33**, 327–337.
- 21 J. Liang, X. Li, K. R. Adair and X. Sun, *Acc. Chem. Res.*, 2021, **54**, 1023–1033.
- 22 S. Wang, Q. Bai, A. M. Nolan, Y. S. Liu, S. Gong, Q. Sun and Y. F. Mo, *Angew. Chem., Int. Ed.*, 2019, **58**, 8039–8043.
- 23 X. N. Li, J. W. Liang, J. Luo, M. N. Banis, C. H. Wang, W. H. Li, S. X. Deng, C. Yu, F. P. Zhao, Y. F. Hu, T. K. Sham, L. Zhang, S. Q. Zhao, S. G. Lu, H. Huang, R. Y. Li, K. R. Adair and X. L. Sun, *Energy Environ. Sci.*, 2019, **12**, 2665–2671.
- 24 X. N. Li, J. W. Liang, N. Chen, J. Luo, K. R. Adair, C. H. Wang, M. N. Banis, T. K. Sham, L. Zhang, S. Q. Zhao, S. G. Lu, H. Huang, R. Y. Li and X. L. Sun, *Angew. Chem., Int. Ed.*, 2019, **58**, 16427–16432.
- 25 G. Kresse and J. Furthmuller, *Phys. Rev. B: Condens. Matter Mater. Phys.*, 1996, **54**, 11169–11186.
- 26 M. Ernzerhof and G. E. Scuseria, *J. Chem. Phys.*, 1999, **110**, 5029–5036.
- 27 B. Hammer, L. B. Hansen and J. K. Norskov, *Phys. Rev. B: Condens. Matter Mater. Phys.*, 1999, **59**, 7413–7421.
- 28 A. Jain, S. P. Ong, G. Hautier, W. Chen, W. D. Richards, S. Dacek, S. Cholia, D. Gunter, D. Skinner, G. Ceder and K. A. Persson, *APL Mater.*, 2013, **1**, 011002.
- 29 A. V. Krugau, O. A. Vydrov, A. F. Izmaylov and G. E. Scuseria, *J. Chem. Phys.*, 2006, **125**, 224106.
- 30 A. Togo and I. Tanaka, *Scr. Mater.*, 2015, **108**, 1–5.
- 31 S. Muy, J. C. Bachman, L. Giordano, H. H. Chang, D. L. Abernathy, D. Bansal, O. Delaire, S. Hori, R. Kanno, F. Maglia, S. Lupart, P. Lamp and Y. Shao-Horn, *Energy Environ. Sci.*, 2018, **11**, 850–859.
- 32 H. M. Chen, L. L. Wong and S. Adams, *Acta Crystallogr., Sect. B: Struct. Sci., Cryst. Eng. Mater.*, 2019, **75**, 18–33.
- 33 G. Henkelman, B. P. Uberuaga and H. Jonsson, *J. Chem. Phys.*, 2000, **113**, 9901–9904.
- 34 S. Nosé, *J. Chem. Phys.*, 1984, **81**, 511–519.
- 35 X. He, Y. Zhu, A. Epstein and Y. Mo, *npj Comput. Mater.*, 2018, **4**, 1–9.
- 36 S. Arrhenius, *Z. Phys. Chem.*, 1889, **4**, 96–116.
- 37 Y. Wang, W. D. Richards, S. P. Ong, L. J. Miara, J. C. Kim, Y. F. Mo and G. Ceder, *Nat. Mater.*, 2015, **14**, 1026–1031.
- 38 Z. M. Xu, X. Chen, R. H. Chen, X. Li and H. Zhu, *npj Comput. Mater.*, 2020, **6**, 1–8.
- 39 Z. M. Xu and H. Zhu, *Chem. Mater.*, 2020, **32**, 4618–4626.
- 40 Y. Qie, S. Wang, S. J. Fu, H. H. Xie, Q. Sun and P. R. Jena, *J. Phys. Chem. Lett.*, 2020, **11**, 3376–3383.
- 41 W. D. Richards, T. Tsujimura, L. J. Miara, Y. Wang, J. C. Kim, S. P. Ong, I. Uechi, N. Suzuki and G. Ceder, *Nat. Commun.*, 2016, **7**, 1–8.
- 42 S. P. Ong, W. D. Richards, A. Jain, G. Hautier, M. Kocher, S. Cholia, D. Gunter, V. L. Chevrier, K. A. Persson and G. Ceder, *Comput. Mater. Sci.*, 2013, **68**, 314–319.
- 43 S. Muy, J. Voss, R. Schlem, R. Koerver, S. J. Sedlmaier, F. Maglia, P. Lamp, W. G. Zeier and Y. Shao-Horn, *iScience*, 2019, **16**, 270–282.
- 44 W. D. Richards, T. Tsujimura, L. J. Miara, Y. Wang, J. C. Kim, S. P. Ong, I. Uechi, N. Suzuki and G. Ceder, *Nat. Commun.*, 2016, **7**, 1–8.